Published in final edited form as:
*Appl Opt*. 2012 July 10; 51(20): 4627–4637.

# Monte Carlo model of the penetration depth for polarization gating spectroscopy: influence of illumination-collection geometry and sample optical properties

**Andrew J. Gomes**[1], **Vladimir Turzhitsky**[2], **Sarah Ruderman**[1], and **Vadim Backman**[1,*]

[1]Department of Biomedical Engineering, Northwestern University, Evanston, Illinois 60218, USA

[2]Biomedical Imaging and Spectroscopy Laboratory, Departments of Medicine and Obstetrics and Gynecology and Reproductive Biology, Beth Israel Deaconess Medical Center, Harvard University, Boston, Massachusetts 02215, USA

## Abstract

Polarization-gating has been widely used to probe superficial tissue structures, but the penetration depth properties of this method have not been completely elucidated. This study employs a polarization-sensitive Monte Carlo method to characterize the penetration depth statistics of polarization-gating. The analysis demonstrates that the penetration depth depends on both the illumination-collection geometry [illumination-collection area ($R$) and collection angle ($\theta_c$)] and on the optical properties of the sample, which include the scattering coefficient ($\mu_s$), absorption coefficient ($\mu_a$), anisotropy factor ($g$), and the type of the phase function. We develop a mathematical expression relating the average penetration depth to the illumination-collection beam properties and optical properties of the medium. Finally, we quantify the sensitivity of the average penetration depth to changes in optical properties for different geometries of illumination and collection. The penetration depth model derived in this study can be applied to optimizing application-specific fiber-optic probes to target a sampling depth of interest with minimal sensitivity to the optical properties of the sample.

## 1. Introduction

Optical interrogation of tissue structure and function has found several applications in biomedical diagnostics, particularly in the diagnosis of precancerous lesions. Carcinomas, including colon cancer and the majority of other cancers, arise from the epithelium in their earliest stages, and are localized to a few hundred micrometers thick mucosal layer. Since light normally diffuses several millimeters/centimeters into tissue (depending on wavelength and optical properties), it is crucial for these applications to ensure that light is preferentially collected from the diagnostic layer of interest by use of depth selective instrumentation and analysis.

Several optical technologies have been developed to selectively probe the superficial layers of tissue. Methods such as optical coherence tomography and confocal microscopy [1] can image tissue structures from several micrometers to 1–2 mm deep into tissue. Differential path-length spectroscopy has been incorporated into a fiber-optic probe to quantify mucosal optical properties [2,3]. In addition, researchers have investigated controlling the sampling depth by altering the illumination-collection geometry via multiple source-detector



*Corresponding author: v-backman@northwestern.edu.

separations [4,5], variable aperture techniques [6,7], angled illumination-collection [8–14], and variable overlap of illumination-collection regions [15,16]. These methods have proven successful in diagnosing epithelial lesions including those in the bronchial, oral, and other types of mucosae [2,17].

A method known as polarization-gating has been widely implemented to selectively probe different penetration depths [18–24]. Polarization-gating relies on the observation that light depolarizes as it undergoes scattering while traversing a medium. The cross-polarized signal $I_{\perp}$, copolarized signal $I_{\parallel}$, and differential polarization-gated signal $I_{\parallel} - I_{\parallel}$ measure progressively shallower tissue depths [25]. Polarization-gating has been incorporated into fiber-optic probes allowing for depth selective measurements *in vivo* [17,25,26]. In particular, we have previously utilized polarization-gating to show that early precancerous alterations in hemoglobin concentration are present at relatively shallow penetration depths (~100–150 μm) but absent at larger penetration depths (>200 μm) [27,28]. The localized nature of these physical changes underscores the penetration depth as an important parameter to take into consideration in the design of clinical biophotonic systems. In addition, there has been growing interest in modeling the light distribution and penetration depth of polarized light in turbid media using polarization-sensitive Monte Carlo (MC) analysis [25,29–33].

In this paper, we present our detailed, quantitative investigation of polarization-gating by means of polarized light MC simulations that incorporate the size of the illumination and collection areas ($R$), the collection angle ($\theta_c$), the anisotropy factor ($g$) of the medium, and the scattering and absorption coefficients of the medium ($\mu_s$, $\mu_a$, respectively). MC simulations are used to quantify the effects of both the optical properties and illumination-collection geometry on the penetration depth statistics of the differential polarization-gated signal. We then develop a novel mathematical expression that functionally relates the mean penetration depth to the sample optical properties and the illumination-collection geometry. Finally, we calculate the sensitivity of the mean penetration depth to sample optical properties for different geometries. Our results can be used to design polarization-gated illumination-collection geometries with optimum combinations of penetration depth and sensitivity of the penetration depth to the sample optical properties for the application of interest.

## 2. Material and Methods

### A. Polarized Light Monte Carlo (MC) Model

Publicly available polarized light meridian plane MC algorithms developed by Ramella-Roman *et al.* [34,35] were used to simulate the propagation and collection of polarized light. The implementation of this algorithm to track photons as functions of polarization, radius, $\theta_c$, and maximum depth travelled ($z$) has been described in detail by Turzhitsky *et al.* [25]. The index of refraction of the sample medium was assumed to be 1.33, and the surrounding environment was either assigned an index of refraction of 1 (air) to simulate a noncontact measurement or 1.52 to mimic the case when contact measurements are taken with a probe having a glass lens as in our previous clinical studies [27,28]. Reflection, refraction, and alteration of the Stokes vector at the sample/environment interface was computed using Snell's law and the Stokes formalism of the Fresnel equations [36].

Furthermore, this study investigated the influence of the type of phase function employed. In conventional MC simulations, either the Mie or Henyey-Greenstein phase function is used to describe the scattering properties of the medium. These phase functions assume that scattering occurs from discrete particles when in reality the refractive index distribution of biologicial tissue is spatially continuous. To better approximate scattering from biological

tissue, we used a phase function derived from the Whittle–Matérn refractive index correlation function to define the scattering properties of the medium. The Whittle–Matérn correlation function is a three-parameter model given by the equation

$$B_n(r) \propto dn^2 \frac{2^{5/2-m}}{|\Gamma(m-(3/2))|}\left(\frac{r}{l_c}\right)^{m-3/2} K_{m-3/2}\left(\frac{r}{l_c}\right). \quad (1)$$

The parameters $dn^2$, $l_c$, and $m$ denote the variance of the refractive index fluctuations, the index correlation distance, and the shape of refractive index correlation function, respectively, while $K_\upsilon(.)$ represents the modified Bessel function of the second kind. The spectral density $\Phi$ at spatial frequency $\kappa$ can be calculated from the Fourier transform of $B_n(r)$ yielding

$$\Phi_n(\kappa) = \frac{dn^2 l_c^3 \Gamma(m)(1+\kappa^2 l_c^2)^{-m}}{\pi^{3/2}|\Gamma(m-(3/2))|}. \quad (2)$$

The spectral density operates on the incident Stokes vector via the scattering Mueller matrix. First, the relation between the scattered Stokes vector $S_s$ and initial Stokes vector $S_o$ is

$$S_s = R(\gamma)M(\theta)R(\phi)S_o, \quad (3)$$

where $R(\gamma)$ and $R(\Phi)$ are rotations into the meridian and scattering planes, respectively, and $M(\theta)$ is the single-scattering Mueller matrix with $\theta$ being the angle between incident and scattered wave vectors [34]. For weakly scattering media, the scattering matrix is related to the spectral density [37,38]:

$$M(\theta) = \frac{\pi}{4}k^4\Phi_n\left(2k\sin\frac{\theta}{2}\right)\begin{bmatrix} m_{11}(\theta)=1+\cos^2(\theta) & m_{12}(\theta)=\cos^2(\theta)-1 & 0 & 0 \\ m_{21}(\theta)=m_{12}(\theta) & m_{22}(\theta)=m_{11}(\theta) & 0 & 0 \\ 0 & 0 & m_{33}(\theta)=2\cos\theta & 0 \\ 0 & 0 & 0 & m_{44}(\theta)=m_{33}(\theta) \end{bmatrix}. \quad (4)$$

The phase function $F(\theta, \phi) = M(\theta)R(\phi)$ for an incident Stokes vector $[I_o Q_o U_o V_o]$ can then be expressed in terms of the elements of the Mueller matrix:

$$F(\theta,\phi) = \frac{\pi}{4}k^4\Phi_n\left(2k\sin\frac{\theta}{2}\right)\begin{pmatrix} m_{11}(\theta)I_o + [m_{12}(\theta)(Q_o\cos 2\phi + U_o\sin 2\phi)] + \\ [m_{13}(\theta)(U_o\cos 2\phi - Q_o\sin 2\phi)] + m_{14}(\theta)V_o \end{pmatrix}. \quad (5)$$

In our MC simulations, $g$ and $m$ were varied, and this uniquely determined a value of $l_c$ [39]. The Stokes vectors of each photon packet were tracked and incoherently summed into corresponding bins of radius ($r$), collection angle ($\theta_c$), and maximum depth travelled ($z$), giving the response to an input pencil beam. Mueller matrix multiplication was used to obtain the output intensity after a polarizer was oriented at 0° or 90° ($I_\parallel$ or $I_\perp$, respectively) with respect to the incident polarization. Convolution was employed to extend the beam from an infinitely narrow source to a circular illumination spot with finite area and radius $R$. The main objective of this study was to quantify the penetration depth behavior of the differential polarization-gated signal $\Delta I(r, z) = I_\parallel(r, z) - I_\perp(r, z)$. To accomplish this, for a given $\theta_c$, the differential signal intensity was integrated from 0 to $R$, giving the penetration depth profile $\Delta I(z)$ for the differential signal. It was found that physical penetration depth could be scaled by the parameter $\mu_t' = \mu_s(1-g)+\mu_a$. Thus the average optical penetration depth ($\tau' = \langle z\mu_t' \rangle$) was determined from the first moment of the depth profile as

$$\tau' = \frac{\sum_{z=0}^{N} z\mu_t' \Delta I(z\mu_t')}{\sum_{z=0}^{N} \Delta I(z\mu_t')}, \quad (6)$$

where $N$ is the maximum depth reached by the photons. This average depth was recorded for different $R\mu_t'$, $\theta_c$, $g$, $\mu_a$, and $m$.

### B. MC Simulations

The geometry of the MC simulations is depicted in Fig. 1. A total of at least $10^8$ photons ($\lambda$ = 632.8 nm) were launched into the sample as a pencil beam for each simulation of illumination-collection geometry and sample optical properties. A series of simulations were performed with various combinations of optical properties. The specific optical properties tested included $g$ = [0.75, 0.8, 0.85, 0.9, 0.93], $m$ = [1.1, 1.3, 1.5, 1.8, 2, 3], $\mu_a/\mu_s$ = [0, 0.007, 0.014, 0.021, 0.042, 0.083, 0.016], and $R\mu_s$ = [1, 3, 5, 7, 9, 11, 13, 15, 17, 19]. The scattering coefficient did not need to be varied, because due to the scaling property of MC [40], there is a unique penetration depth output (when scaled to $\mu s$) for each $R\mu_s$ irrespective of the individual values of $R$ and $\mu_s$. Since $R$ can be modified by convolution in the postprocessing of a single MC run, a total of 210 MC simulations were needed to encompass all the possible optical property combinations. These simulations were repeated with the Mie phase function, of which only 42 simulations were needed, since there was no $m$ parameter to vary.

### C. Development of Penetration Depth Equation

Analysis of the MC simulations revealed that the average penetration depth of the polarization-gated signal behaved according to following stretched exponential expression:

$$\tau' = a(1 - \exp(-b(R\mu_t')^c)). \quad (7)$$

Conceptually, the parameter $a$ represents the saturation point of the stretched exponential curve, parameter the $b$ represents the rate at which the curve reaches the saturation point, and the parameter $c$ quantifies the deviation of the curve from a pure exponential function ($c$ = 1). We will refer to the parameters $a$, $b$, and $c$ as the saturation, rate, and stretch parameters, respectively. Since the individual scattering properties $\mu_s$, $\mu_a$, and $g$ are encapsulated in the single variable $\mu_t'$, we only needed to model the parameters $a$, $b$, and $c$ as functions of $\theta_c$ to completely describe the penetration depth behavior as a function of both illumination-collection geometry and sample optical properties. We found that $a$, $b$, and $c$ could be modeled as simple linear functions of $\theta_c$.

### D. Experimental Verification of Penetration Depth Expression

We created thin polydimethylsiloxane (PDMS) based phantoms that varied in thickness to test the mathematical expression we developed. To create one phantom with a graded thickness, a small amount of resin consisting of a scattering agent mixed with PDMS was cured between two glass plates with a spacer between the plates on one edge. Either titanium dioxide ($TiO_2$) powder (Sigma-Aldrich, St Louis, Missouri) or melamine microspheres (microParticles, GmbH, Germany)) was selected as the scattering agent and embedded within PDMS (Slygard 184; Dow Corning Corp, Midland, Michigan). PDMS consists of a two-part kit with a base and cross-linking agent. For our experimental protocol, we first added 6.5 mg of $TiO_2$ per gram of PDMS base agent. Then, to ensure the $TiO_2$ particles were uniformly distributed, the solution was sonicated for 4–5 h. Next, the cross-linking

agent was added to the solution in a 1:10 ratio by weight, and the final solution degassed in a vacuum oven at room temperature for 25 min to remove all air from the sample. The resultant mixture was then poured between the glass plates and cured at 60 °C for 1 hour and left at room temperature overnight. Once cured, a solution of clear PDMS was then layered on top of the scattering phantom, and again set overnight to cure. This second layer created an index matched boundary to minimize Fresnel reflections. The final phantomhad a wedge shape with a linear increase in thickness across the length of the phantom as illustrated in Fig. 2(a). Reflectance and transmittance measurements were taken from the phantom with an integrating sphere, and the inverse adding-doubling method described by Prahl [41] was used to extract the optical properties of the phantom from these measurements. The inverse adding-doubling method assumes a Henyey-Greenstein phase function. The measured optical properties were $\mu_s = 16\ \text{mm}^{-1}$ and $g = 0.64$. Measurements were then taken with a polarization-gated fiber-optic probe having $R = 400\ \mu\text{m}$ and $\theta_c = 14°$. A ZEMAX (ZEMAX, Bellevue, Washington) ray tracing of the light paths through the probe is shown in Fig. 2(b). The surface of the medium and the illumination-collection fibers are separated by a gradient refractive index (GRIN) lens whose purpose is to ensure that the illumination and collection beams overlap on the medium's surface as shown in Fig. 2(b). This mimics the geometry of the MC simulations depicted in Fig. 1. The probe is symmetric such that there is another collection fiber on the other side of the illumination fiber shown in Fig. 2(b). One collection fiber collects backscattered light polarized parallel to the illumination beam, while the other collects light polarized perpendicular to the illumination beam. Further details of the probe design may be found in [25]. The signal intensities $I_{\parallel}$ and $I_{\perp}$ were recorded as a function of distance along the incline of the phantom from the thinnest section to the thickest section as shown in Fig. 2(c). Knowing the total length (5 cm) and height (1 mm) of the incline, we geometrically mapped the distance along the phantom to the thickness of the sample being interrogated by the probe. Thus we obtained signal intensities that were functions of sample thickness. The average penetration depth can be derived from these measurements using the analysis given by Turzhitsky *et al.* [25]. In brief, the signal intensity versus the sample thickness curve can be interpreted as the cumulative probability distribution for the penetration depth. The derivative of this curve, properly normalized, is then the penetration depth probability distribution, and the average penetration depth can be extracted by taking the first moment of this distribution. We repeated this procedure for another phantom, except that we used melamine microspheres with a diameter of 1.6 ± 0.04 μm as the scattering agent instead of $TiO_2$. The optical properties for this particular wedge were $g = 0.9$ and $\mu_s = 500\ \text{cm}^{-1}$.

## 3. Results and Discussion

### A. Effect of Illumination-Collection Geometry on the Mean Penetration Depth of the Differential Polarization-Gated Signal

We investigated two main parameters that can be used to characterize the illumination-collection geometry: the radius of the illumination-collection aperture ($R$) and the collection angle ($\theta_c$). To investigate the effect of $R$ on the mean penetration depth, we varied $R$ while keeping other optical and geometry parameters constant: $\theta_c = 0$–18°, and $m = 1.5$. For each $R$, we determined the mean penetration depth ($\tau'$) defined as the product of the physical penetration depth ($z$) and $\mu_t'$. Figure 3(a) shows the dependence of $\tau'$ on the dimensionless parameter $R\mu_t'$ for three different $g$'s and two different $\mu_a$'s. The individual curves corresponding to different $g$'s and $\mu a$'s overlap with each other, confirming that both the average penetration depth and the illumination-collection area can be scaled by $\mu_t'$. In other words, there is a unique $\tau'$ for each $R\mu_t'$ irrespective of the individual values of $\mu_s$, $\mu_a$, and $g$.

Therefore, the penetration depth relation with $R\mu_t'$ can be modeled by a stretched exponential function of the form

$$\tau' = a(1 - \exp(-b(R\mu_t')^c)).$$

The $R^2$ of the stretched exponential fit to the data in Fig. 3(a) is 0.99, indicating excellent agreement. The increase in $\tau'$ with $R\mu_t'$ agrees with our previous studies in polarization-gated spectroscopy as well as other studies on variable-aperture techniques. The qualitative reason for the dependence on $R$ is that a photon that traverses deeper into the sample is more likely to exit at a greater lateral distance from its point of origin compared to a photon that only infiltrates near the sample surface. Limiting $R$ excludes deep-travelling photons and consequently reduces $\tau$. In Eq. (7), we developed an explicit relationship between $R$ and $\tau'$ that can be utilized in fiber-optic probe and system design. For example, in a fiber-optic probe, $R$ can be controlled by the numerical aperture of the illumination-collection fibers or by increasing the focal length of the lens. In a benchtop system, a simple iris aperture can be employed to control $R$. After fitting the stretched exponential expression to 175 different combinations of $g$, $\theta_c$, and, $\mu_a/\mu_s$, the average $R^2$ was 0.997 with a minimum value of 0.93, indicating that stretch exponential expression was a highly accurate and robust fit to the MC results. In Subsection 3.D, we illustrate how the fitting parameters of the stretched exponential can be modeled as functions of the collection angle to derive a general equation for the mean penetration depth. We next investigated the effect of the collection angle ($\theta_c$) on the mean penetration depth. As discussed in Section 2, the exit angle of each photon with respect to the surface normal was recorded and stored in bins of 0–18, 18–36, 36–54, 54–72, and 72–9°. Figure 3(b) demonstrates that $\tau'$ decreases monotonically as $\theta_c$ is increased for $g$ = 0.9, $R\mu_t$ = 9, $\mu_a$ = 0, and $m$ = 1.5. This trend is maintained for other combinations of optical properties (data not shown). This finding agrees with previous research, which found that the average penetration depth of both polarized and depolarized photons decreased with $\theta_c$ [25]. These findings suggest that the penetration depth can be tuned by selecting the appropriate $\theta_c$. In a fiber-optic probe design, controlling the distance between illumination-collection fibers determines $\theta_c$ while in a benchtop system a Fourier lens can be used to achieve angle-resolved detection [23].

### B. Influence of the Phase Function on the Penetration Depth

As stated in Subsection 2.B, we performed MC simulations using both the Mie and Whittle–Matérn phase functions. Figure 4(a) compares the average penetration depth computed with each type of phase function as a function of $\theta_c$ for a specific set of optical properties ($R\mu_t$ = 9, $g$ = 0.75, $\mu_a$ = 0, $m$ = 1.5). Here $m$ = 1.5 corresponds to the Henyey-Greenstein phase function [39]. The penetration depth decreases with $\theta_c$ for both phase functions, but the magnitude of the penetration depth is different between the phase functions, particularly for $\theta_c$ = 0–18 and 72–90° (23 and 36% difference, respectively). Moreover, the penetration depth decreases more quickly with $\theta_c$ for the Whittle–Matérn phase function. Both the magnitude and behavior of the penetration depth depends on the type of phase function employed. Since the Whittle–Matérn function more realistically represents the properties of biological tissue, we decided to focus on this phase function in our penetration depth equation development. In order to proceed with the Whittle-Matérn phase function, we first needed to ascertain the effect of the parameter $m$ on the average penetration depth. This parameter describes the shape of the refractive index correlation function. In biological tissue, $m$ typically varies between 1 and 2 with $m$ < 1.5 corresponding to a mass fractal index distribution. In Fig. 4(b), we plot the dependence of $\tau$ on $m$ and demonstrate that they are independent with <1% variation over the range of $m$. We therefore omitted $m$ from the penetration depth equation.

### C. Effect of the Scattering and Absorption Properties on the Penetration Depth

We next investigated the impact of the sample optical properties on $\tau$. The relationship between the scattering coefficient $\mu_s$ and $\tau'$ is contained in Fig. 3(a) due to the scaling property of MC, and the relationship is also formalized by the stretched exponential expression. Analysis of this expression shows that the penetration depth decreases with $\mu_s$. This is because increasing $\mu_s$ effectively reduces the scaled illumination-collection area, which has already been shown in Subsection 3.B to reduce $\tau'$. Next, we plotted the relationship between the anisotropy factor $g$ and $\tau(\langle z\mu_s \rangle)$ shown in Fig. 5(a). The value $\tau$ instead of $\tau'$ was chosen to maintain independence between the $x$ and $y$ axes. The penetration depth clearly increases with $g$ and quite rapidly for $g > 0.85$. This is consistent with both the observation that light polarization is preserved for longer light paths for higher $g$ and that light is more forward directed in a high $g$ sample. Finally, we analyzed the influence of $\mu_a$ on $\tau$ in Fig. 5(b), where it is shown that $\tau$ decreases with $\mu_a$. This is expected in an absorbing medium since photons are less likely to travel long light paths due to the increased probability of being absorbed. This set of results demonstrates that the optical properties play a significant role in determining the penetration depth of the differential polarization-gated signal. Consequently, the mathematical expression derived in the next subsection incorporates the above sample optical properties to determine the average penetration depth.

### D. MC Derived Equation for the Penetration Depth

We have so far shown how each individual element of the illumination-collection geometry and sample optical properties control the penetration depth of polarization-gated spectroscopy. Our next goal was to integrate all these relationships into a single equation that can predict $\tau'$ based on the illumination-collection geometry of a detection system and the optical properties of a phantom or tissue sample. The discovery that the average penetration depth and the illumination-collection area scale with $\mu_t'$ greatly simplified this process because the variable $\mu_t'$ allowed us to package the effects of three optical property parameters ($\mu_s$, $\mu_a$, and $g$) into a single scaling variable. The only variable missing from the stretched exponential expression in Eq. (7) is the effect of $\theta_c$. To include this variable, we modeled the saturation, rate, and stretch parameters as linear functions of $\theta_c$ as illustrated in Fig. 6. Figure 6 demonstrates that this linear approximation is valid for all three parameters with an $R^2$ greater than 0.93 such that these parameters can be expressed in the form $x_1\theta_c + x_2$. The values of the linear fitting coefficients for stretched exponential parameters $x_1$ and $x_2$ are summarized in Table 1. We next compared the output of the stretched exponential equation ($\tau'_{\text{equation}}$) in Eq. (7) using the coefficients in Table 1 to the actual $\tau'$ s from the MC simulations ($\tau'_{\text{MC}}$). This comparison is illustrated in Fig. 7(a), where $\tau'_{\text{equation}}$ is plotted versus $\tau'_{\text{MC}}$. Most of the data points lie within close proximity to the $\tau'_{\text{equation}}=\tau'_{\text{MC}}$ ideal line. There was an average of a 5% percent error between $\tau'_{\text{equation}}$ and $\tau'_{\text{MC}}$. To further investigate the accuracy of $\tau'_{\text{equation}}$, we plot the dependence of the percent error between $\tau'_{\text{equation}}$ and $\tau'_{\text{MC}}$ versus $\mu_a/\mu_s$ for different $\theta_c$ in Fig. 7(b). Above $\mu_a/\mu_s = 0.02$, the percent error increases monotonically for all $\theta_c$. In addition, Fig. 7(b) demonstrates that an error of <10% can be maintained for $\mu_a/\mu_s < 0.15$ and a $\theta_c < 45°$. Outside these bounds, an error <10% can still be achieved, but it will depend on the combination of $\mu_a/\mu_s$ and $\theta_c$ chosen. There was no significant dependence of the percent error on $R\mu_t$ or $g$ (data not shown).

### E. Experimental Verification of Penetration Depth Equation

To show that that the MC-derived penetration depth equation can be applied to experimental constructs, we carried out a series of measurements on two-phantoms. These phantoms were

constructed to have different optical properties and thus different penetration depths. Details of the phantom construction and experimental procedure are discussed in Section 2. Measurements were taken along the inclined surface of each phantom with a polarization-gated spectroscopy probe as documented in Section 2. This experimentally derived value ($\tau'_{\text{equation}}$) was then compared with $\tau'_{\text{equation}}$ by inputting the optical properties of the phantom and geometry of the probe into the penetration depth equation. An $m$ value of 1.5 was used for the MC derived equation since this $m$ value corresponds to the Henyey-Greenstein phase function employed by the inverse-adding doubling method to obtain the phantom optical properties [42]. For the $TiO_2$ and melamine phantoms tested, the differences between $\tau'_{\text{equation}}$ and $\tau'_{\text{experiment}}$ were 8% and 16%, respectively. These experimental measurements confirm that the expression can be used to reliably estimate the average penetration depth for a given system geometry and sample.

### F. Penetration Depth Sensitivity to Sample Optical Properties

The mathematical expression for the penetration depth lends itself to several advantages. For instance, it can be readily manipulated to determine the sensitivity of the penetration depth to changes in the optical properties of the sample. This is an important parameter to consider because an ideal clinical system would consistently target the same diagnostic depth even with perturbations of the optical properties in the measurement area. An optimum sensitivity would minimize both intrapatient and interpatient variability and therefore maximize clinical performance. For our sensitivity calculations, we are interested in the physical penetration depth. $z=\tau'/\mu_t'$. We define the sensitivity $S$ to be

$$S=\left|\frac{\Delta z/z}{\Delta \mathrm{OP}/\mathrm{OP}}\right|, \quad (8)$$

where $OP$ is the magnitude of the optical property of interest, $\frac{\Delta z}{\Delta \mathrm{OP}}$ is interpreted as the local derivative about $OP$, and $z$ is the average penetration depth at $OP$. In brief, $S$ gives the fractional change in the penetration depth given a fractional change in the optical property of interest. For example, an $S = 0.1$ would mean that the penetration depth changes by 1% given a 10% alteration in $OP$. In Fig. 8, we plot $S$ versus $R$ for different $\theta_c$ and with each panel corresponding to a different $OP$ ($\mu_t'$, $\mu_s$, $\mu_a$, and $g$). In particular, Fig. 8(a) shows the sensitivity to $\mu_t'$ as a function of $R\mu_t'$ and $\theta_c$. The family of curves shown in Fig. 8(a) is universal in the sense that for a particular $\theta_c$, there is a unique $S$ for each $R\mu_t'$. Thus to identify the effect of alterations in $\mu_s$, $\mu_a$, and/or $g$ on the average penetration depth, one only need to calculate the corresponding change in $\mu_t'$ given $R\mu_t'$ and $\theta_c$. For visualization purposes, we have also illustrated the individual sensitivities to $\mu_s$, $g$, and $\mu_a$ in Figs. 8(b)–8(d), respectively. One conclusion to be drawn from Fig. 8 is that selecting the smallest $R$ and largest $\theta_c$ minimizes $S$ for each of the optical properties tested. If the goal is to reduce penetration depth variability due to alterations in optical properties, then selecting a probe with the smallest illumination-collection area and largest collection angle would be optimal.

## 4. Conclusions

We have studied the influence of the illumination-collection geometry and sample optical properties on the penetration depth of the differential polarization-gated signal using MC simulations. Furthermore, we have condensed the results of our studies into a single mathematical expression relating the penetration depth to the geometry and optical properties. The expression demonstrates that the penetration depth can be tuned by both the

illumination-collection area and the collection angle. Use of this equation has several advantages. Once implemented in a computer program, the effect of a specific illumination-collection geometry and set of optical properties can be evaluated in a matter of seconds versus the hours it may take for independent MC simulations. Additionally, this equation can be manipulated to investigate other parameters of interest. In this paper, we analyzed the sensitivity of the penetration depth to the sample optical properties and concluded that this sensitivity can be minimized by choosing a large collection angle and small illumination-collection area.

The validity of the penetration depth expression is limited by the absorption coefficient and the collection angle. As stated in the results, an error of less than 10% between the MC results and the mathematical expression can be maintained for $\mu_a/\mu_s < 0.15$ and a $\theta_c < 45°$. There is evidence that the absorption coefficient condition is generally satisfied in tissue. Measurements of $\mu_a/\mu_s$ in colonic mucosa revealed $\mu_a/\mu_s \approx 0.016$ at a wavelength of 532 nm, while $\mu_a/\mu_s$ in the oral mucosa is estimated to be less than 0.05 [43,44]. We therefore believe that that the expression can be used across a wide range of tissue, though care must be taken to ensure the absorption coefficient condition is satisfied, especially in cases where the absorption coefficient is known to be high, such as at the site of a tumor.

We used a homogeneous model in our simulations even though tissue is inhomogeneously structured. It is common in the literature to use homogenous models as a starting point since incorporating all the complexities of tissue structure would be untenable. There is also theoretical justification to for using fixed optical properties instead of spatially varying ones. Even if the optical properties within a medium are spatially varying, an average optical property for the medium can be determined [45]. For example, for a sample having $N$ regions, each with a different scattering coefficient ($\mu_s$) value, the effective scattering coefficient of the medium can be written as $\mu_{s,\text{medium}} = \sum_{i=1}^{N} p_i \mu_{s,i}$ where $p_i$ is the volume fraction of the $i$th region and $\mu_{s,i}$ is the scattering coefficient of the $i$th region. Similar equations exist for the anisotropy factor and absorption coefficient. Thus our results on homogeneous samples should apply to heterogeneous samples provided that the effective optical properties are specified. Nevertheless, it is an area of future study to investigate the penetration depth in layered heterogeneous media. The expression developed in this paper offers a recipe from which application-specific systems or probes with engineered penetration depths can be constructed. The depth-localized nature of diagnostic changes in tissue, especially those associated with early carcinogenesis, has been well documented. We have previously shown that polarization-gated spectroscopy was more sensitive to early increases in blood supply in an azoxymethane animal model of colon carcinogenesis than the conventional Western blot analysis for hemoglobin, precisely because polarization-gated spectroscopy could target the most diagnostic depth [46]. More recently, we have documented that increases in microvessel density measured by immunohistochemical staining was most pronounced in the mucosa rather than submucosa of this animal model [47]. We further noted in human *in vivo* studies that increases in blood supply associated with premalignant colonic lesions was most pronounced at an average depth of ~100 μm but rapidly dissipated until almost no effect at all was noted at a depth >200 μm. The need to target a precise tissue depth is not limited to the colon. For example, Terry *et al.* used angle-resolved low coherence interferometry to demonstrate that elevation of nuclear diameter associated with dysplasia in Barrett's esophagus was only detectable at a depth of 200–300 μm and not observable at 0–100 μm or 100–200 μm [48]. These studies collectively highlight the clinical and biological importance of developing optical technologies to interrogate the appropriate tissue depth for the application of interest. Our mathematical expression offers a method to construct optical systems that fulfill this need.

In conclusion, we utilized a polarized MC model to investigate the effect of optical properties and system geometry on the average penetration depth of the polarization-gated signal. These investigations are condensed into a mathematical expression that can be manipulated to estimate both the average depth and the sensitivity of that depth to changes in optical properties for a given sample and illumination-collection geometry. We anticipate that is expression will be useful for rational and application-centered design of polarization-gated biophotonic systems.

## References


1. Pawley, JB.; Masters, BR. Handbook of Biological Confocal Microscopy. 3rd ed. Springer: 2006.
2. Amelink A, Sterenborg HJ, Bard MP, Burgers SA. In vivo measurement of the local optical properties of tissue by use of differential path-length spectroscopy. Opt. Lett. 2004; 29:1087–1089. [PubMed: 15181994]
3. Amelink A, Sterenborg HJ. Measurement of the local optical properties of turbid media by differential path-length spectroscopy. Appl. Opt. 2004; 43:3048–3054. [PubMed: 15176191]
4. Pfefer TJ, Schomacker KT, Ediger MN, Nishioka NS. Multiple-fiber probe design for fluorescence spectroscopy in tissue. Appl. Opt. 2002; 41:4712–4721. [PubMed: 12153108]
5. Zhu C, Liu Q, Ramanujam N. Effect of fiber optic probe geometry on depth-resolved fluorescence measurements from epithelial tissues: a Monte Carlo simulation. J. Biomed. Opt. 2003; 8:237–247. [PubMed: 12683849]
6. Pfefer TJ, Matchette LS, Ross AM, Ediger MN. Selective detection of fluorophore layers in turbid media: the role of fiber-optic probe design. Opt. Lett. 2003; 28:120–122. [PubMed: 12656504]
7. Quan L, Ramanujam N. Relationship between depth of a target in a turbid medium and fluorescence measured by a variable-aperture method. Opt. Lett. 2002; 27:104–106. [PubMed: 18007726]
8. Wang AM, Bender JE, Pfefer J, Utzinger U, Drezek RA. Depth-sensitive reflectance measurements using obliquely oriented fiber probes. J. Biomed. Opt. 2005; 10:44017. [PubMed: 16178650]
9. Skala MC, Palmer GM, Zhu C, Liu Q, Vrotsos KM, Marshek-Stone CL, Gendron-Fitzpatrick A, Ramanujam N. Investigation of fiber-optic probe designs for optical spectroscopic diagnosis of epithelial pre-cancers. Lasers Surg. Med. 2004; 34:25–38. [PubMed: 14755422]
10. Reif R, A'Amar O, Bigio IJ. Analytical model of light reflectance for extraction of the optical properties in small volumes of turbid media. Appl. Opt. 2007; 46:7317–7328. [PubMed: 17932546]
11. Pfefer TJ, Agrawal A, Drezek RA. Oblique-incidence illumination and collection for depth-selective fluorescence spectroscopy. J. Biomed. Opt. 2005; 10:44016. [PubMed: 16178649]
12. Nieman L, Myakov A, Aaron J, Sokolov K. Optical sectioning using a fiber probe with an angled illumination-collection geometry: evaluation in engineered tissue phantoms. Appl. Opt. 2004; 43:1308–1319. [PubMed: 15008534]
13. Lin SP, Wang L, Jacques SL, Tittel FK. Measurement of tissue optical properties by the use of oblique-incidence optical fiber reflectometry. Appl. Opt. 1997; 36:136–143. [PubMed: 18250654]
14. Nieman LT, Jakovljevic M, Sokolov K. Compact beveled fiber optic probe design for enhanced depth discrimination in epithelial tissues. Opt. Express. 2009; 17:2780–2796. [PubMed: 19219183]
15. Arifler D, Schwarz RA, Chang SK, Richards-Kortum R. Reflectance spectroscopy for diagnosis of epithelial precancer: model-based analysis of fiber-optic probe designs to resolve spectral information from epithelium and stroma. Appl. Opt. 2005; 44:4291–4305. [PubMed: 16045217]
16. Schwarz RA, Arifler D, Chang SK, Pavlova I, Hussain IA, Mack V, Knight B, Richards-Kortum R, Gillenwater AM. Ball lens coupled fiber-optic probe for depth-resolved spectroscopy of epithelial tissue. Opt. Lett. 2005; 30:1159–1161. [PubMed: 15945140]
17. Nieman LT, Kan CW, Gillenwater A, Markey MK, Sokolov K. Probing local tissue changes in the oral cavity for early detection of cancer using oblique polarized reflectance spectroscopy: a pilot clinical trial. J. Biomed. Opt. 2008; 13:024011. [PubMed: 18465974]
18. Anderson RR. Polarized light examination and photography of the skin. Arch. Dermatol. 1991; 127:1000–1005. [PubMed: 2064396]

19. Backman V, Gurjar R, Badizadegan K, Itzkan I, Dasari RR, Perelman LT, Feld MS. Polarized light scattering spectroscopy for quantitative measurement of epithelial cellular structures in situ. IEEE J. Sel. Top. Quantum Electron. 1999; 5:1019–1026.
20. Demos SG, Alfano RR. Optical polarization imaging. Appl. Opt. 1997; 36:150–155. [PubMed: 18250656]
21. Jacques SL, Ramella-Roman JC, Lee K. Imaging skin pathology with polarized light. J. Biomed. Opt. 2002; 7:329–340. [PubMed: 12175282]
22. Jacques SL, Roman JR, Lee K. Imaging superficial tissues with polarized light. Lasers Surg. Med. 2000; 26:119–129. [PubMed: 10685085]
23. Kim YL, Yang L, Wali RK, Roy HK, Goldberg MJ, Kromin AK, Kun C, Backman V. Simultaneous measurement of angular and spectral properties of light scattering for characterization of tissue microarchitecture and its alteration in early precancer. IEEE J. Sel. Top. Quantum Electron. 2003; 9:243–256.
24. Siegel MP, Kim YL, Roy HK, Wali RK, Backman V. Assessment of blood supply in superficial tissue by polarization-gated elastic light-scattering spectroscopy. Appl. Opt. 2006; 45:335–342. [PubMed: 16422163]
25. Turzhitsky VM, Gomes AJ, Kim YL, Liu Y, Kromine A, Rogers JD, Jameel M, Roy HK, Backman V. Measuring mucosal blood supply in vivo with a polarization-gating probe. Appl. Opt. 2008; 47:6046–6057. [PubMed: 19002229]
26. Myakov A, Nieman L, Wicky L, Utzinger U, Richards-Kortum R, Sokolov K. Fiber optic probe for polarized reflectance spectroscopy in vivo: design and performance. J. Biomed. Opt. 2002; 7:388–397. [PubMed: 12175288]
27. Gomes AJ, Roy HK, Turzhitsky V, Kim Y, Rogers JD, Ruderman S, Stoyneva V, Goldberg MJ, Bianchi LK, Yen E, Kromine A, Jameel M, Backman V. Rectal mucosal microvascular blood supply increase is associated with colonic neoplasia. Clin. Cancer Res. 2009; 15:3110–3117. [PubMed: 19383816]
28. Roy HK, Gomes A, Turzhitsky V, Goldberg MJ, Rogers J, Ruderman S, Young KL, Kromine A, Brand RE, Jameel M, Vakil P, Hasabou N, Backman V. Spectroscopic microvascular blood detection from the endoscopically normal colonic mucosa: biomarker for neoplasia risk. Gastroenterology. 2008; 135:1069–1078. [PubMed: 18722372]
29. Dogariu M, Asakura T. Photon pathlength distribution from polarized backscattering in random media. Opt. Eng. 1996; 35:2234–2239.
30. Guo X, Wood MF, Vitkin A. Monte Carlo study of pathlength distribution of polarized light in turbid media. Opt. Express. 2007; 15:1348–1360. [PubMed: 19532365]
31. Guo X, Wood MFG, Vitkin A. A Monte Carlo study of penetration depth and sampling volume of polarized light in turbid media. Opt. Commun. 2008; 281:380–387.
32. Liu Y, Kim Y, Li X, Backman V. Investigation of depth selectivity of polarization gating for tissue characterization. Opt. Express. 2005; 13:601–611. [PubMed: 19488390]
33. Liu Y, Kim YL, Backman V. Development of a bioengineered tissue model and its application in the investigation of the depth selectivity of polarization gating. Appl. Opt. 2005; 44:2288–2299. [PubMed: 15861834]
34. Ramella-Roman J, Prahl S, Jacques S. Three Monte Carlo programs of polarized light transport into scattering media: part I. Opt. Express. 2005; 13:4420–4438. [PubMed: 19495358]
35. Ramella-Roman JC, Prahl SA, Jacques SL. Three Monte Carlo programs of polarized light transport into scattering media: part II. Opt. Express. 2005; 13:10392–10405. [PubMed: 19503254]
36. Jaillon F, Saint-Jalmes H. Description and time reduction of a Monte Carlo code to simulate propagation of polarized light through scattering media. Appl. Opt. 2003; 42:3290–3296. [PubMed: 12793409]
37. Moscoso M, Keller JB, Papanicolaou G. Depolarization and blurring of optical images by biological tissue. J. Opt. Soc. Am. A Opt. Image Sci. Vis. 2001; 18:948–960. [PubMed: 11318346]

38. Radosevich A, Rogers J, Turzhitsky V, Mutyal N, Yi J, Roy H, Backman V. Polarized enhanced backscattering spectroscopy for characterization of biological tissues at sub-diffusion length-scales. IEEE J. Sel. Top. Quantum Electron. 2011; 18:1313–1325.
39. Rogers JD, Capoglu IR, Backman V. Nonscalar elastic light scattering from continuous random media in the Born approximation. Opt. Lett. 2009; 34:1891–1893. [PubMed: 19529738]
40. Graaff R, Koelink MH, de Mul FFM, Zijistra WG, Dassel ACM, Aarnoudse JG. Condensed Monte Carlo simulations for the description of light transport. Appl. Opt. 1993; 32:426–434. [PubMed: 20802708]
41. Prahl SA, van Gemert MJ, Welch AJ. Determining the optical properties of turbid mediaby using the adding-doubling method. Appl. Opt. 1993; 32:559–568. [PubMed: 20802725]
42. Turzhitsky V, Radosevich A, Rogers JD, Taflove A, Backman V. A predictive model of backscattering at sub-diffusion length scales. Biomed. Opt. Express. 2010; 1:1034–1046. [PubMed: 21258528]
43. Pavlova I, Weber CR, Schwarz RA, Williams MD, Gillenwater AM, Richards-Kortum R. Fluorescence spectroscopy of oral tissue: Monte Carlo modeling with site-specific tissue properties. J. Biomed. Opt. 2009; 14:014009. [PubMed: 19256697]
44. Wei HJ, Xing D, Lu JJ, Gu HM, Wu GY, Jin Y. Determination of optical properties of normal and adenomatous human colon tissues in vitro using integrating sphere techniques. World J. Gastroenterol. 2005; 11:2413–2419. [PubMed: 15832410]
45. Graaff R, Aarnoudse JG, Zijp JR, Sloot PM, de Mul FF, Greve J, Koelink MH. Reduced light-scattering properties for mixtures of spherical particles: a simple approximation derived from Mie calculations. Appl. Opt. 1992; 31:1370–1376. [PubMed: 20720767]
46. Wali RK, Roy HK, Kim YL, Liu Y, Koetsier JL, Kunte DP, Goldberg MJ, Turzhitsky V, Backman V. Increased microvascular blood content is an early event in colon carcinogenesis. Gut. 2005; 54:654–660. [PubMed: 15831911]
47. Tiwari AK, Crawford SE, Radosevich A, Wali RK, Stypula Y, Kunte DP, Mutyal N, Ruderman S, Gomes A, Cornwell ML, Cruz MD, Brasky J, Gibson TP, Backman V, Roy HK. Neo-angiogenesis and the premalignant microcirculatory augmentation of early colon carcinogenesis. Cancer Lett. 2011; 306:205–213. [PubMed: 21493000]
48. Terry NG, Zhu Y, Rinehart MT, Brown WJ, Gebhart SC, Bright S, Carretta E, Ziefle CG, Panjehpour M, Galanko J, Madanick RD, Dellon ES, Trembath D, Bennett A, Goldblum JR, Overholt BF, Woosley JT, Shaheen NJ, Wax A. Detection of dysplasia in Barrett's esophagus with in vivo depth-resolved nuclear morphology measurements. Gastroenterology. 2011; 140:42–50. [PubMed: 20854820]

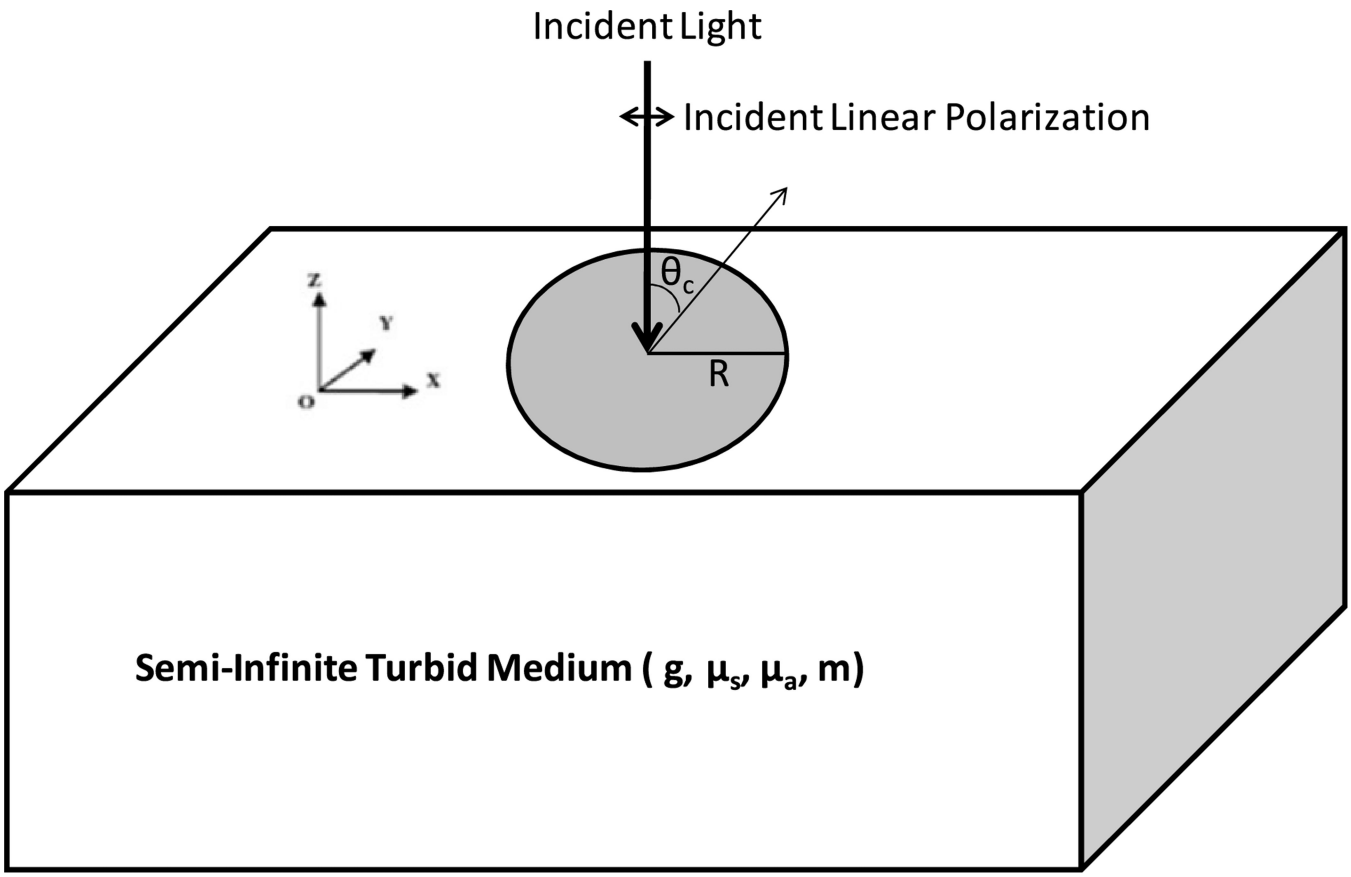


**Fig. 1.**

Geometry of the MC simulations. Pencil beam of linearly polarized light is incident in the *z* direction upon a turbid medium whose optical properties are characterized by the anisotropy factor (*g*), scattering and absorption coefficients ($\mu_s$ and $\mu_a$), and shape of the refractive index correlation function (*m*). The exit angle of the photons collected ($\theta_c$) is recorded and convolution is used to extend the infinitely narrow source to an illumination-collection aperture of radius *R*.

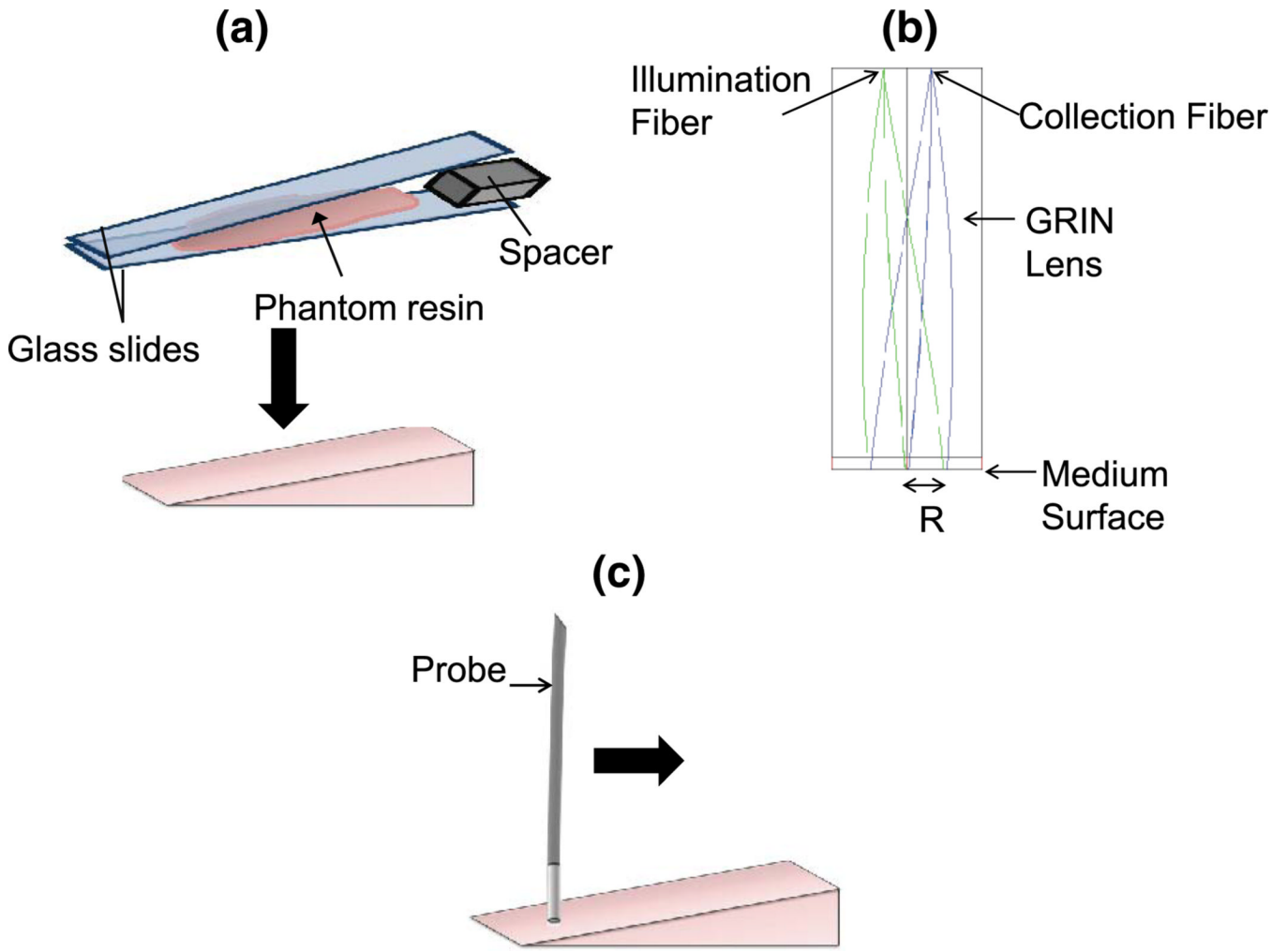


**Fig. 2.**

(Color online) Polarization-gated measurements with a fiber-optic probe on a wedge shaped phantom to experimentally measure the penetration depth. (a) A wedge shaped phantom was constructed by curing PDMS resin between two glass slides separated by a 5 mm metal spacer; (b) a ray tracing of the illumination and collection beams through the polarization-gated probe. The illumination and collection areas overlap on the medium surface. The design of the probe is symmetric such that there is another collection fiber on the other side of the illumination fiber; (c) measurements were taken on the wedge phantom with the probe across the length of the phantom corresponding to different thicknesses.

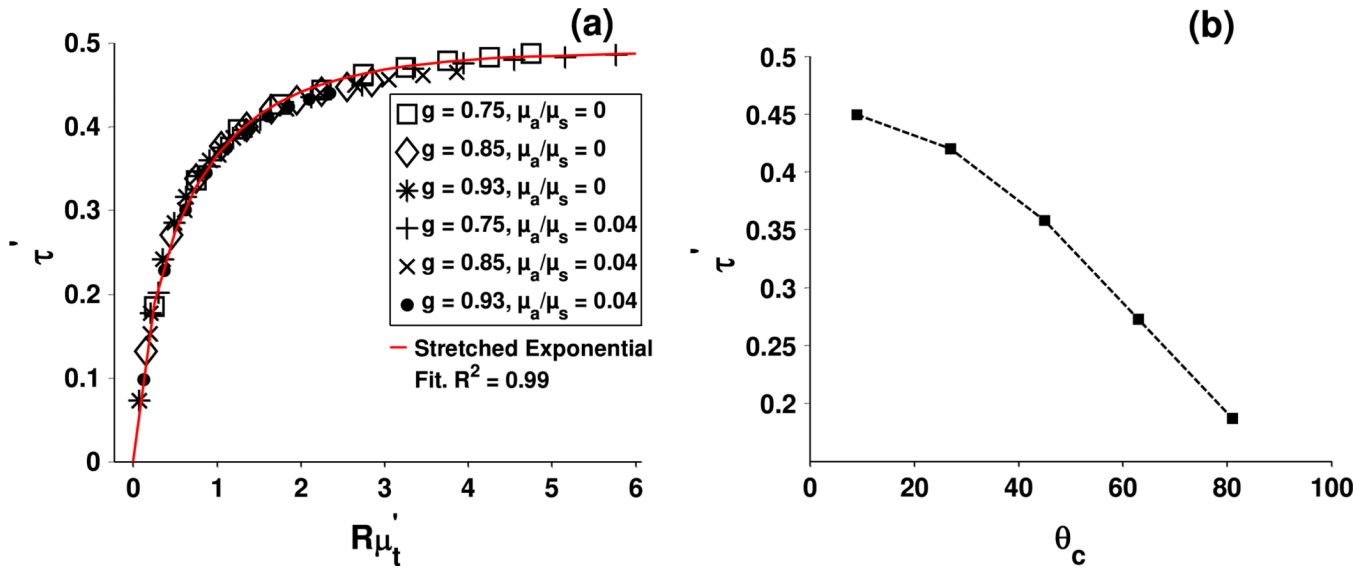


**Fig. 3.**

(Color online) Polarized MC results of the differential average penetration depth $\tau'$ as a function of the illumination and collection geometry: (a) influence of the illumination/collection radius $R\mu_t'$ with the collection angle $\theta_c$ = 0–18°; (b) and the effect of $\theta_c$ with $R\mu_t'$=9. The fixed values of the other sample parameters were $\mu_a$ = 0, $g$ = 0.9, and $m$ = 1.5.

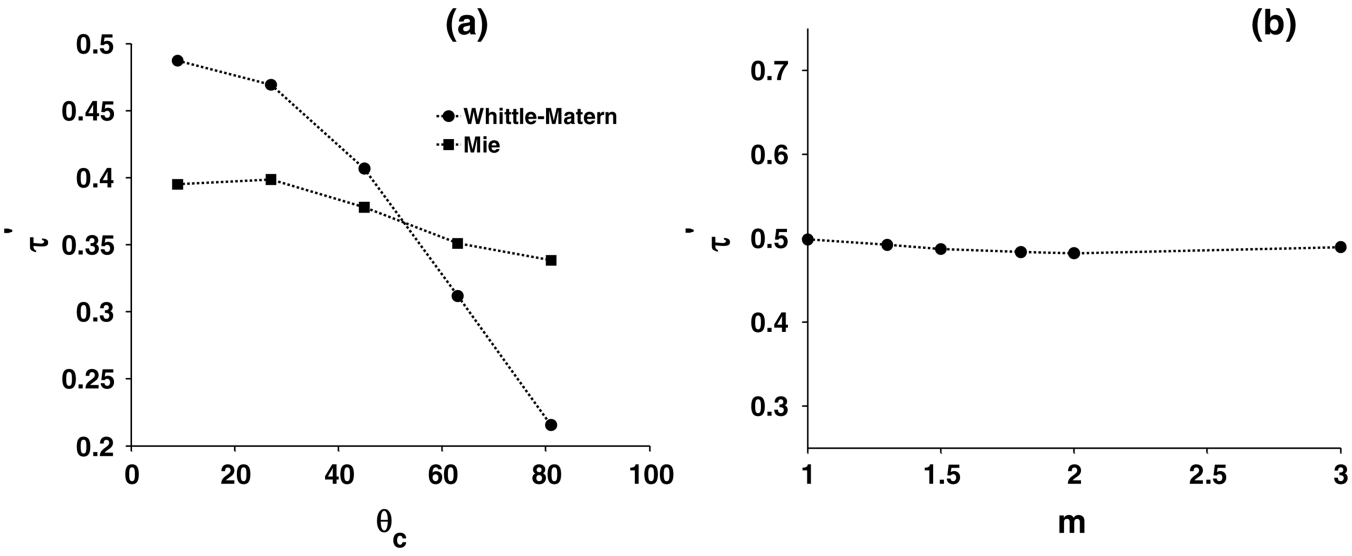


**Fig. 4.**

Polarized MC results summarizing the influence of the phase function on the average penetration depth. (a) Comparison of the average penetration depth derived from MC Mie and Whittle–Matérn phase functions for different $\theta_c$ and $m = 1.5$ in the Whittle–Matérn case; (b) Influence of the shape of the refractive index correlation function, parameterized by $m$ in the Whittle–Matérn model, on the average penetration depth for $\theta_c = 0$–18°. The fixed values of the other sample and geometry parameters were $g = 0.75$, $\mu_a = 0$, and $R\mu_t = 9$.

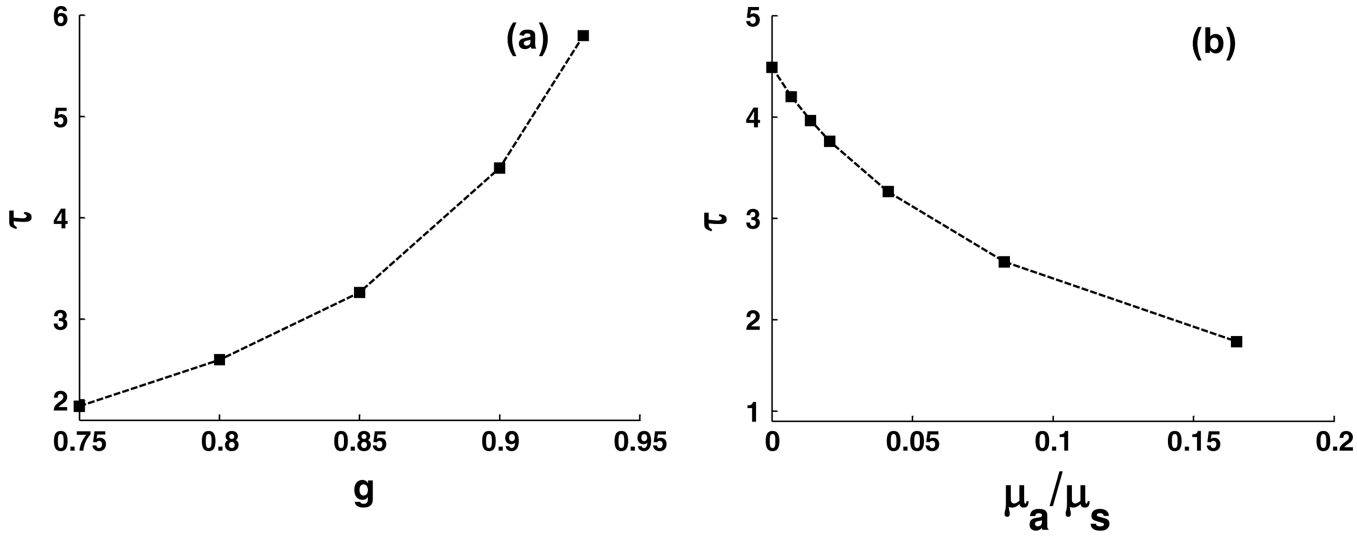


**Fig. 5.**

Polarized MC results illustrating the effect of sample optical properties on the average penetration depth: (a) influence of the anisotropy factor $g$ on $\tau$ for $\mu_a = 0$; and (b) influence of the absorption coefficient $\mu_a$ on $\tau$ for $g = 0.9$. Note that the dependence of $T$ on the scattering coefficient $\mu_s$ is already explicit in Fig. 1(a). The fixed values of the other sample and geometry properties were $R\mu_t = 9$, $\theta_c = 0$–18°, and $m = 1.5$.

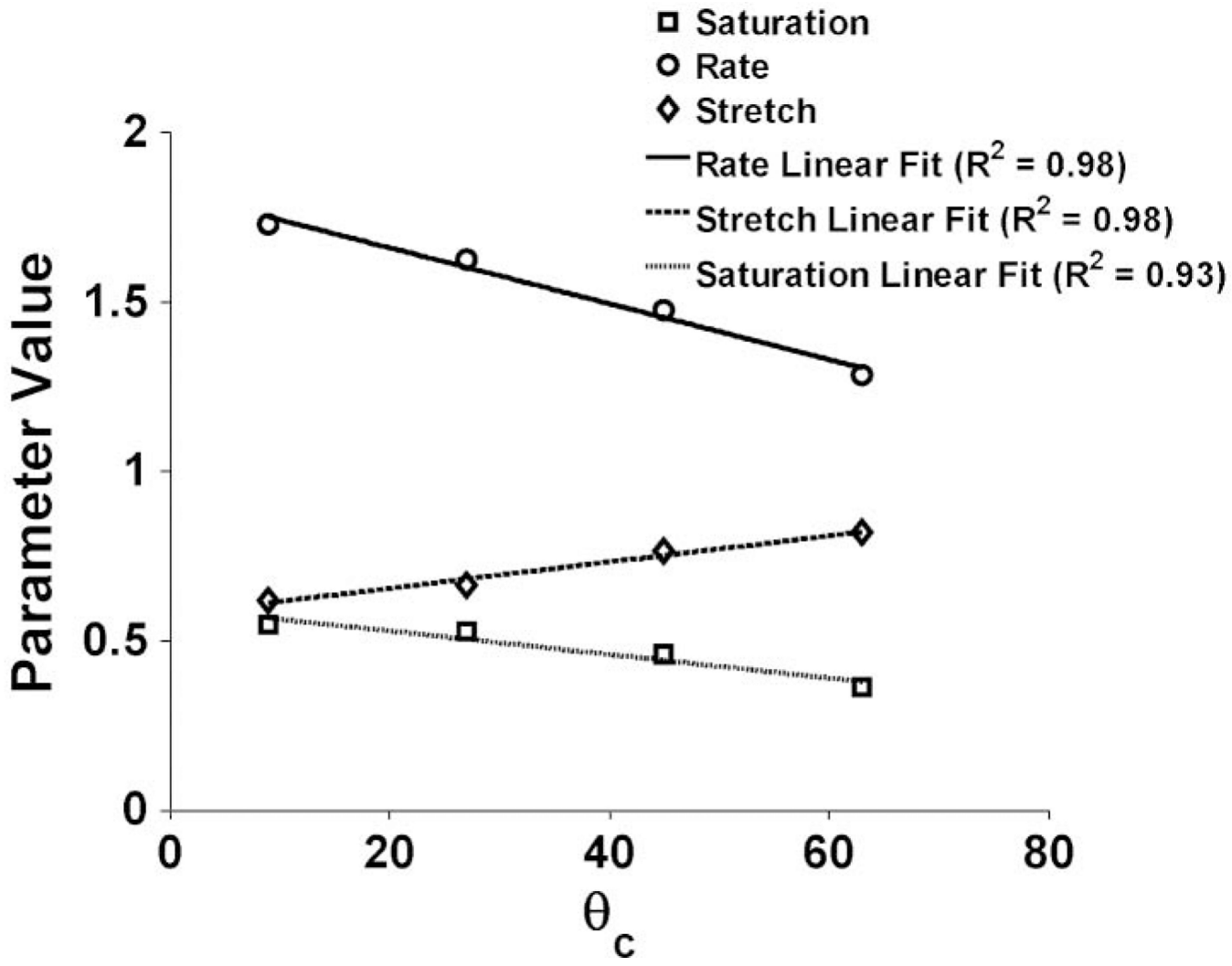


**Fig. 6.**
Linear behavior of stretched exponential parameters as a function of $\theta_c$.

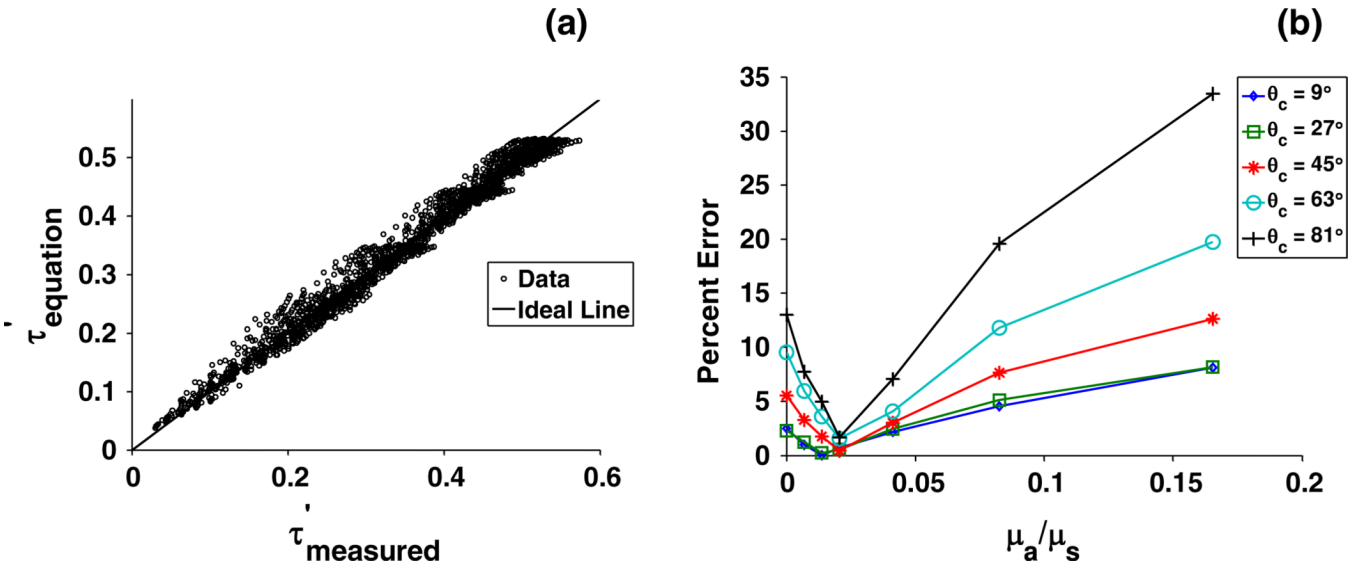


**Fig. 7.**

(Color online) Comparison of the average penetration depth determined by the analytical model equation ($\tau'_{equation}$) versus the average penetration depth calculated from the MC simulations ($\tau'_{MC}$). Data are for a wide range of sample properties and illumination-collection geometries that have been listed in Section 2. (a) $\tau'_{equation}$ plotted versus $\tau'_{MC}$ with the line of unity showed for comparison purposes. The average percent error across all data points and the ideal line is 5%; (b) the percentage error between $\mu_t'$ as a function of $\mu_a$ and $\theta_c$ with $g$ = 0.93, $R\mu_t$ = 9, and $m$ = 1.5.

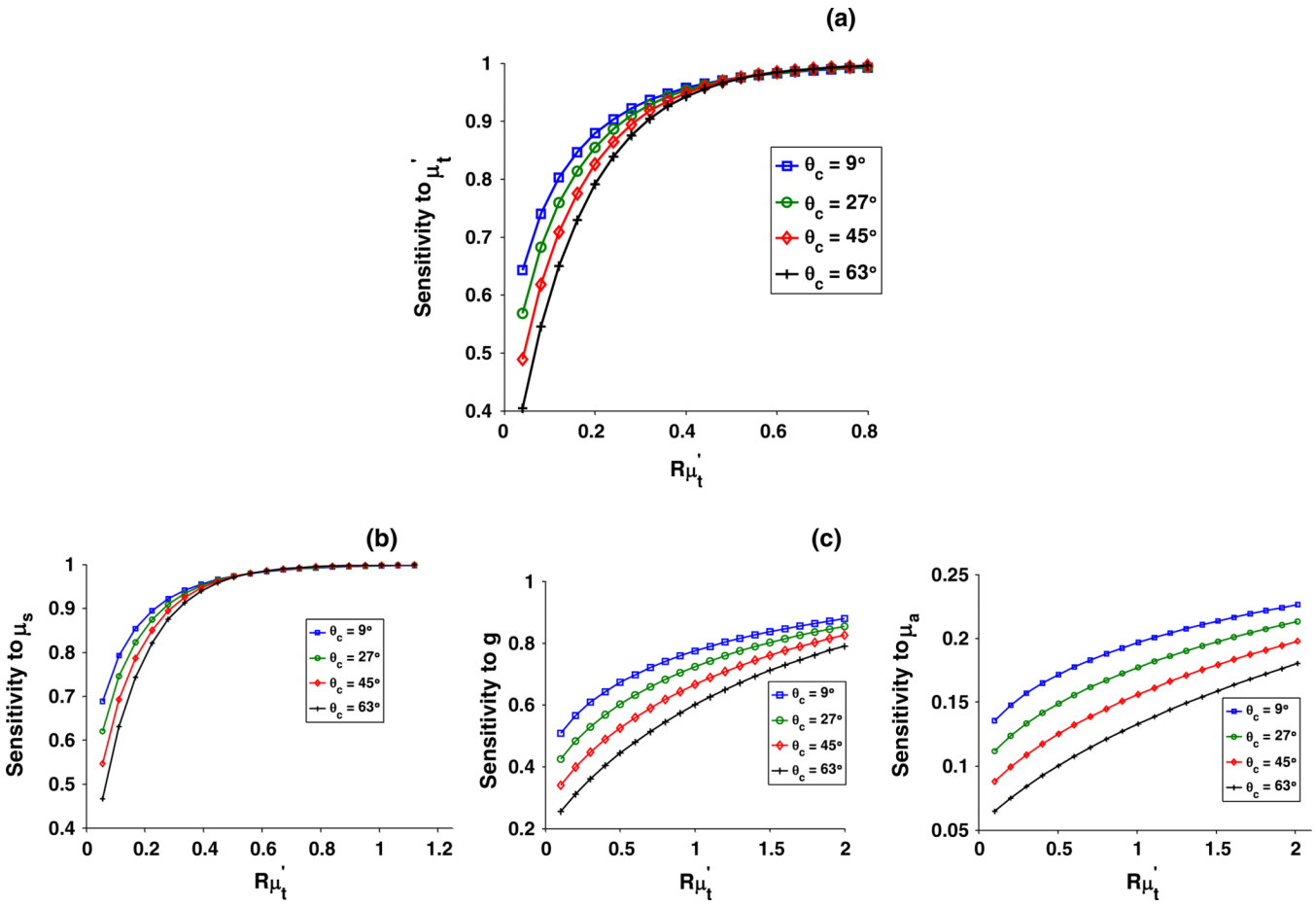


**Fig. 8.**

(Color online) Sensitivity (S) of the average penetration depth to the sample optical properties for different illumination/collection geometries. (a) Penetration depth sensitivity to the total reduced scattering coefficient $\mu_t'$ as a function of $R$ and $\theta_c$ with $u_a = 0$, $g = 0.9$ and $m = 1.5$; (b) penetration depth sensitivity to the scattering coefficient $\mu_s$ as a function of $R$ and $\theta_c$ with $u_a = 0$, $g = 0.9$ and $m = 1.5$. The derivative is evaluated about $\mu_s = 20\ \text{mm}^{-1}$; (c) depth sensitivity to the anisotropy factor $g$ as a function of $R$ and $\theta_c$ with $\mu_a = 0$, and $m = 1.5$. The derivative is evaluated about $g = 0.9$; (d) sensitivity to the absorption coefficient $\mu_a$ with $g = 0.9$ and $m = 1.5$ and the derivative calculated about $\mu_a/\mu_s = 0.04$.

**Table 1**

Linear Fitting Coefficients

| Parameter | $x_1$ | $x_2$ |
|---|---|---|
| *a* | −0.00347 | 0.598 |
| *b* | −0.008237 | 1.824 |
| *c* | 0.00387 | 0.577 |